Estimating the nature and the horizontal and vertical positions of 3D magnetic sources using Euler deconvolution

Felipe F. Melo[1], Valeria C. F. Barbosa[1], Leonardo Uieda[1], Vanderlei C. Oliveira Jr.[1], and João B. C. Silva[2]

ABSTRACT

We have developed a new method that drastically reduces the number of the source location estimates in Euler deconvolution to only one per anomaly. Our method employs the analytical estimators of the base level and of the horizontal and vertical source positions in Euler deconvolution as a function of the x- and y-coordinates of the observations. By assuming any tentative structural index (defining the geometry of the sources), our method automatically locates plateaus, on the maps of the horizontal coordinate estimates, indicating consistent estimates that are very close to the true corresponding coordinates. These plateaus are located in the neighborhood of the highest values of the anomaly and show a contrasting behavior with those estimates that form inclined planes at the anomaly borders. The plateaus are automatically located on the maps of the horizontal coordinate estimates by fitting a first-degree polynomial to these estimates in a moving-window scheme spanning all estimates. The positions where the angular coefficient estimates are closest to zero identify the plateaus of the horizontal coordinate estimates. The sample means of these horizontal coordinate estimates are the best horizontal location estimates. After mapping each plateau, our method takes as the best structural index the one that yields the minimum correlation between the total-field anomaly and the estimated base level over each plateau. By using the estimated structural index for each plateau, our approach extracts the vertical coordinate estimates over the corresponding plateau. The sample means of these estimates are the best depth location estimates in our method. When applied to synthetic data, our method yielded good results if the bodies produce weak- and mid-interfering anomalies. A test on real data over intrusions in the Goiás Alkaline Province, Brazil, retrieved sphere-like sources suggesting 3D bodies.

INTRODUCTION

In the middle of the last century, many governmental agencies opened a new era in the acquisition of a huge amount of aeromagnetic data, which in turn propelled the development of automatic aeromagnetic interpretation methods such as Euler deconvolution. Historically, Thompson (1982) proposed an Euler-based profile depth estimation method called "EULDPH" and Reid et al. (1990) implemented the grid extension suggested by Thompson and coined the term "Euler deconvolution." After the Reid et al. (1990) extension, Euler deconvolution has gained enormous popularity as a semiautomated method to estimate the 3D position of magnetic sources. This popularity is because Euler deconvolution is a fast-processing method that requires no prior knowledge about the anomalous source magnetization, but just its homogeneity in intensity and direction (Barbosa and Silva, 2011).

In Euler deconvolution, a small moving data-window operator is applied in a piecewise way over the whole gridded data set. Using the observations inside the small data window and assuming the geometry of the source, Euler deconvolution estimates the horizontal and vertical source positions by solving a small linear system of equations. This moving data window scheme permits fast interpretations of massive data sets in the presence of interfering signals produced by multiple sources. This moving-data window scheme is one of the reasons why Euler deconvolution became a useful tool in estimating the locations of multiple geologic bodies. However,

this scheme leads to a large number of Euler solutions (Barbosa and Silva, 2011). This scenario is further complicated when the geometry of the source is unknown and when multiple sources with different geometries are present. In these cases, the geometry of the source (related to the structural index) is tentatively assumed by the interpreter and the Euler deconvolution is applied to whole data set. Thus, for each assumed structural index, Euler deconvolution produces a map of source-position estimates. This procedure leads to a set of maps, each one displaying a broad cloud of Euler solutions, rendering nontrivial the interpretation of the locations of multiple geologic bodies. According to Barbosa and Silva (2011), the large number of estimated solutions by Euler deconvolution still remains an operational disadvantage of this method.

To overcome this difficulty, some methods have been developed to select the best Euler solutions and to reduce the number of accepted Euler solutions. Thompson (1982) accepts those Euler solutions displaying small dispersions in depth estimates. Fairhead et al. (1994) accept just the Euler solutions derived from moving data windows located about the maximum of the horizontal gradient of the reduced-to-the-pole anomaly. Mikhailov et al. (2003) reduce the number of acceptable Euler solutions by using a clustering technique based on artificial intelligence. Li (2003) selects a single anomaly and applies the Euler deconvolution to this selected anomaly by using a single data window. FitzGerald et al. (2004) present a comprehensive review of practical techniques that are usually used to distinguish reliable from spurious Euler solutions. Jekeli (2009) shows that the ad hoc criterion often used to accept Euler solutions (Reid et al., 1990) yields better results than the probabilistically founded test (using the Student and Fisher distributions for random variables) that determines whether an estimate of a parameter is reasonably consistent. Jekeli (2009) proposes a criterion for Euler solution acceptance based on the coefficient of the depth estimates. Ugalde and Morris (2010) filter the coherent Euler solutions by means of a kernel density distribution algorithm and reduce these filtered solutions by using the fuzzy c-means clustering algorithm.

Except for the Fairhead et al. (1994) and the Li (2003) criteria, all other solution acceptance criteria are based on a measure of the tightness of the Euler solutions cluster. Usually, this cluster is also used to select the best geometry of the magnetic source. In practice, several geometries are tentatively assumed, and the one providing the tightest cluster of Euler solutions is selected as the best source geometry.

Silva et al. (2001) showed that the scattering of the Euler solutions in a practical problem is caused both by the choice of the wrong structural index and by the presence of noise in the data. They also pointed out that the criterion for determining the structural index as the tentative value producing the smallest solution scattering is theoretically sound, but occasionally fails because of noise in data. Hence, the widely used Thompson (1982) criterion for accepting Euler solutions may fail. Silva et al. (2001) also answer an intriguing question of Euler deconvolution initially raised by Ravat (1996): Why is the average of the horizontal position estimates less sensitive to the wrong choice of the structural index and/or to noise in the data as compared with the vertical position estimates? Silva et al. (2001) prove that these behaviors follow directly from the symmetry properties of the estimates. They also help us understand that the horizontal position estimates through Euler deconvolution are more robust than the vertical position estimates

because the former are insensitive to the wrong choice of the structural index and to the data noise. Hence, the acceptance criterion of Euler solutions, based on the tight cluster of horizontal and vertical position estimates, may fail mainly because of the larger scattering of the vertical position estimates.

The robustness of the horizontal position estimates by Euler deconvolution is confirmed by Silva and Barbosa (2003) who deduce the analytical estimators of the horizontal and vertical source positions in Euler deconvolution. Silva and Barbosa (2003) also reveal a contrasting behavior of these estimators at the borders and at the neighborhood of the highest absolute values of the anomaly. This differentiated behavior is due to the bias of the horizontal and vertical coordinates estimates. At the borders of the anomaly, the estimates of the horizontal and vertical coordinates are biased toward the respective horizontal and vertical coordinates of the data-window center. Conversely, in the neighborhood of the highest absolute values of the anomaly, the estimates of the horizontal coordinates are good and consistent estimates of the correct source coordinates, defining, in this way, plateau areas. These plateaus are defined in the maps of the horizontal coordinate estimates against the central position of the data window being independent of the assumed structural index and the magnetization direction. These plateaus are also associated with consistent estimates of the vertical coordinate. However, the estimates of the vertical coordinate at these plateaus are very close to the vertical coordinate of the true source if and only if the structural index is correctly assumed.

In this paper, we present a new method for selecting the best Euler solutions by using the theoretical basis proposed by Silva and Barbosa (2003). Our method takes advantage of the contrasting behavior of the Euler solutions at the borders and at the neighborhood of the highest absolute values of the anomaly. It automatically delineates the regions of the magnetic data producing the best Euler solutions, each one associated with an anomalous source. Each region will be an area located at the neighborhood of the highest absolute values of the anomaly where the consistent Euler solutions are produced by Euler deconvolution. These regions are delineated by mapping the plateaus, pointed out by Silva and Barbosa (2003), in the maps of the horizontal coordinate estimates against the central position of the data window. If the sources are horizontally well separated, then these plateaus are also horizontally well separated from each other and thus their horizontal positions can be easily recognized through a cluster analysis. Each subset of horizontal coordinates defining a plateau (and consequently the horizontal position of an anomalous source) is used to pick out the best estimates of the horizontal coordinates by assuming any structural index in Euler deconvolution. Next, for each anomalous source, our approach calculates the means of the best estimates of the horizontal source positions over the associated plateau. For each plateau that is associated with an anomalous source, our method determines the structural index via the Barbosa et al. (1999) method. By using this structural index determined for each plateau, our approach picks out the best estimates of the vertical coordinates over the corresponding plateau. Finally, the mean of the best estimates of the vertical source positions are calculated for each anomalous source.

For each magnetic anomaly, our method provides a single source position. Moreover, the method can estimate the positions of multiple sources, whether they are characterized by the same structural index or not. These assertions are confirmed by tests with synthetic

data. A test on a total-field anomaly collected over mafic-ultramafic alkaline bodies located in the Goiás Alkaline Province, central Brazil, leads to the interpretation of two sphere-like sources whose centers are located at depths of 3 and 3.2 km.

METHODOLOGY

Let's assume a magnetic point (or line) source at the coordinates (x_o, y_o, z_o) referred to a right-hand Cartesian coordinate system with the z-axis pointing downward. The observed total-field anomaly $h \equiv h(x, y, z)$ at the coordinates (x, y, z) produced by this simple magnetic source obeys Euler's 3D equation (Reid et al., 1990). By considering a discrete set of N observations of the total-field anomaly, the classical formulation of Euler deconvolution can be written as a linear system of equations given by

$$x_o \frac{\partial h_i}{\partial x} + y_o \frac{\partial h_i}{\partial y} + z_o \frac{\partial h_i}{\partial z} + \eta b = x_i \frac{\partial h_i}{\partial x} + y_i \frac{\partial h_i}{\partial y} + z_i \frac{\partial h_i}{\partial z} + \eta h_i,$$
$$i = 1, \dots, N, \tag{1}$$

where $h_i \equiv h(x_i, y_i, z_i)$ is the ith observation of the total-field anomaly at the coordinates (x_i, y_i, z_i), b is a base level (i.e., a constant background value) and η is the structural index related to the nature or geometry of the source.

For a given structural index, the Euler deconvolution consists in solving the system of equations 1, in the least-squares sense, for the unknown parameters x_o, y_o, z_o, and b. This procedure leads to a single set of the estimates $\hat{x}_o, \hat{y}_o, \hat{z}_o$, and $\hat{b}$ that would be expected to locate an isolated magnetic source and to estimate the base level. In interpreting noisy and interfering total-field anomalies from a complex geologic setting with multiple sources, the Euler deconvolution uses gridded observations and produces many sets of estimates $\hat{x}_o$, $\hat{y}_o$, $\hat{z}_o$, and $\hat{b}$, each one obtained by using the observations inside a small data window formed by a grid of $NX \times NY$ data points (Figure 1a). Hence, for a given data window the Euler deconvolution obtains the estimates $\hat{x}_o, \hat{y}_o, \hat{z}_o$, and $\hat{b}$ and the next estimates are obtained by shifting the data window with a shift size of one data spacing. This procedure is repeated over the whole data set in a moving-data window scheme. As pointed out by Barbosa and Silva (2011), this procedure has the disadvantage of computing a large number of inconsistent estimated solutions making it difficult to decide on the correct locations of the geologic sources.

By assuming a null base level in equation 1, Silva and Barbosa (2003) deduce the analytical estimators $\hat{x}_o, \hat{y}_o$, and $\hat{z}_o$ (see equations 8–10 in Silva and Barbosa, 2003). The most striking feature of these analytical estimators for parameters x_o, y_o, and z_o is their bias and symmetry properties as a function of the moving-data window position. Silva and Barbosa (2003) proved that, at the anomaly borders, the estimates $\hat{x}_o, \hat{y}_o$, and $\hat{z}_o$ are biased toward the arithmetic averages of the respective x-, y-, and z-coordinates of the center of the moving-data window (Figure 1b). This happens regardless of the assumed structural indices and regardless of the magnetization inclination and declination. Conversely, in the neighborhood of the highest absolute values of the anomaly the estimates $\hat{x}_o, \hat{y}_o$, and $\hat{z}_o$ are approximately constant values defining a plateau (Figure 1b). Specifically, at this plateau, the estimates $\hat{x}_o$ and $\hat{y}_o$ are very close to the respective x- and y-coordinates of the true source, independently of the assumed structural index and independently of the

source magnetization vector. However, the estimates $\hat{z}_o$, on this plateau, are very close to the z-coordinate of the true source only if the assumed structural index is correct; otherwise, the estimates $\hat{z}_o$ will underestimate (or overestimate) the z-coordinate of the true source if the assumed structural index is smaller (or greater) than the correct one.
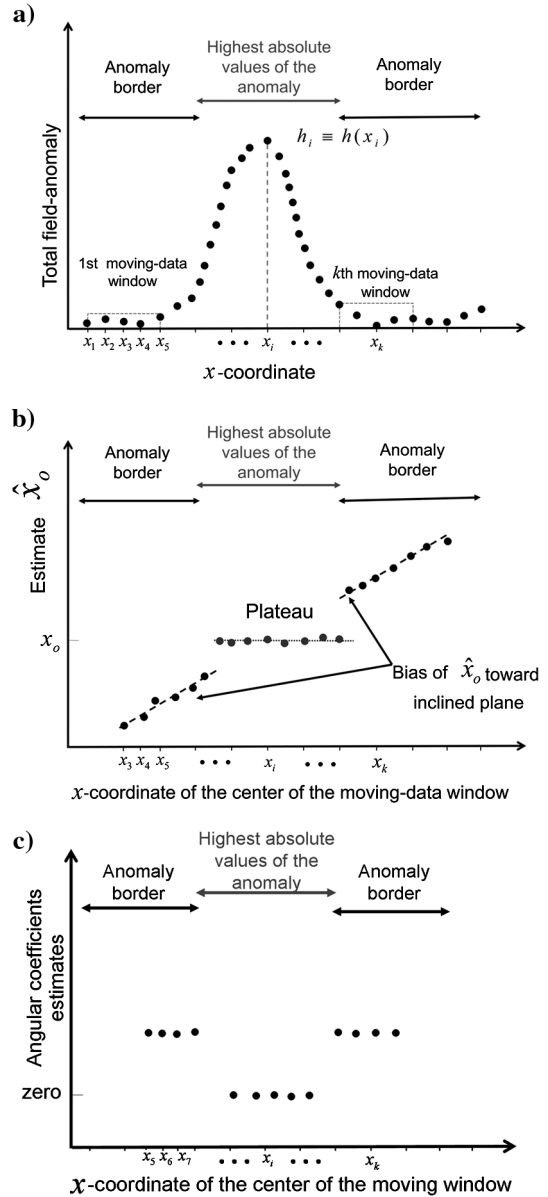

Figure 1. Two-dimensional sketch of the method. (a) The total-field anomaly (dots), where $h_i \equiv h(x_i)$ is the ith observation at the coordinate (x_i). The sketch of the first and kth moving data windows whose centers are x_3 and x_k, respectively. (b) Estimates $\hat{x}_o$ (dots) against the x-coordinate of the center of the moving data window. The estimates $\hat{x}_o$ (black dots) define inclined planes (dashed black lines) at the anomaly borders. The estimates $\hat{x}_o$ (gray dots) define a plateau (stippled gray line) at the neighborhood of the highest absolute values of the anomaly, close to the true position x_o of the source. (c) Angular coefficients estimates against the x-coordinate of the center of the moving window. The place where the angular coefficients estimates are closest to zero identify automatically a plateau of $\hat{x}_o$ in (b).

In this paper, we take advantage of this behavior of the Euler solutions in producing plateaus to compute automatically the best estimates of the horizontal $(\tilde{x}_o, \tilde{y}_o)$ and vertical $(\tilde{z}_o)$ source positions. First, our method selects the best horizontal coordinate estimates $(\tilde{x}_o$ and $\tilde{y}_o)$ in Euler deconvolution for each source by assuming any structural index. Second, it determines the structural index (η) of each source as will be explained below. Finally, the method selects the best depth estimate $(\tilde{z}_o)$ of each source by using the estimated structural index.

Selecting the best horizontal coordinate estimates in Euler deconvolution

The practical procedure to determine the best estimates $\tilde{x}_o$ and $\tilde{y}_o$ is as follows. First, we apply the Euler deconvolution with any structural index. For each position of the moving data window, we produce the plots of $\hat{x}_o$ and $\hat{y}_o$ against the x- and y-coordinates of the center of the moving-data window (Figure 1b). After producing these two plots of $\hat{x}_o$ and $\hat{y}_o$, we automatically identify the plateaus (see next paragraph) and extract the subsets of the $\hat{x}_o$ and $\hat{y}_o$ estimates that fall within the respective plateaus. Then, for these extracted subsets of the $\hat{x}_o$ and $\hat{y}_o$ estimates, we compute the sample means $\tilde{x}_o$ and $\tilde{y}_o$, which will be defined as the best estimates of the horizontal source positions.
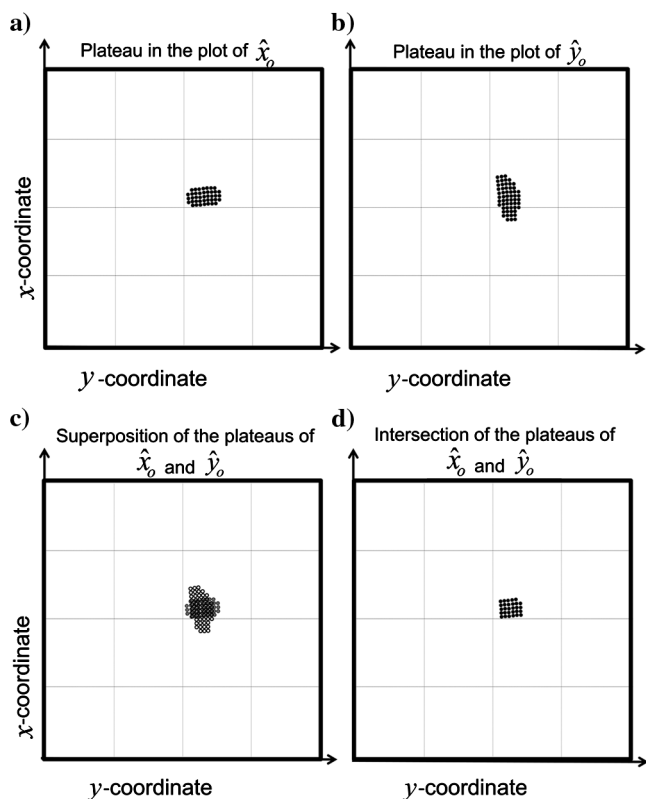

Figure 2. Schematic representation of the positions (subsets of the x- and y-coordinates) of plateau in the maps of (a) $\hat{x}_o$ and (b) $\hat{y}_o$. Superposition (c) and intersection (d) of the pairs of plateaus of $\hat{x}_o$ and of $\hat{y}_o$ shown in (a) and (b), respectively. The best coordinate estimates $\tilde{x}_o$, $\tilde{y}_o$ and $\tilde{z}_o$ in 3D Euler deconvolution are the sample means of the subsets of the estimates $\hat{x}_o$, $\hat{y}_o$ and $\hat{z}_o$ over the respective plateaus in (a), (b), and (d), respectively.

To automatically identify the plateaus in the plots of $\hat{x}_o$ and $\hat{y}_o$, we take advantage of the bias and symmetry properties pointed out by Silva and Barbosa (2003). Graphically, this means that, at the anomaly borders, the estimates $\hat{x}_o$ and $\hat{y}_o$ form inclined planes (Figure 1b). Hence, a crucial point in our method lies in the ability to distinguish plateaus from inclined planes in the plots of $\hat{x}_o$ and $\hat{y}_o$ against the central position of the data window (Figure 1b). Here, to differentiate the plateaus from these inclined planes on the estimates $\hat{x}_o$ and $\hat{y}_o$, our method fits, in the least-squares sense, first-degree polynomials to these estimates. This fitting will be accomplished through a moving-window scheme spanning the maps of the estimates of $\hat{x}_o$ and $\hat{y}_o$ on the plane of the x-coordinates against the y-coordinates of the center of the moving window. This scheme consists in fitting a first-degree polynomial to the subset of the estimates $\hat{x}_o$ and $\hat{y}_o$ defining each moving window (Figure 1b). Next, the estimated angular coefficients of these fitted polynomials are plotted against the center of the moving window (Figure 1c). Then, the places where the corresponding angular coefficients estimates are closest to zero identify the plateaus in the plots of $\hat{x}_o$ and $\hat{y}_o$ automatically. The mathematical and algorithmic details are given in Appendix A.

Selecting the structural index

After identifying the plateaus in the plots of $\hat{x}_o$ and $\hat{y}_o$ and obtaining the best estimates of the horizontal source positions $(\tilde{x}_o$ and $\tilde{y}_o)$, we proceed to determine the best structural index η, and for this purpose we follow the approach proposed by Barbosa et al. (1999). Based on Euler's equation, Barbosa et al. (1999) show that the estimates of the base level $(\hat{b})$, as a function of the center of the moving-data window, are correlated with the observed total-field anomaly (h). If the tentative structural index is greater (or smaller) than the correct one, this correlation is positive (or negative). A minimum correlation between the estimates $\hat{b}$ and h is favored when the correct structural index is assumed.

Here, the practical procedure adopted to determine the best structural index is as follows. We first obtain estimates $\hat{b}$ by using the classical Euler deconvolution for some tentative structural indices. Next, we select the subsets of the total-field anomaly and estimates $\hat{b}$ that approximately fall within the plateaus identified in the plots of $\hat{x}_o$ and $\hat{y}_o$. Finally, for each tentative structural index, we compute the correlation coefficient between these subsets of the total-field anomaly and of the estimates $\hat{b}$. The tentative structural index that produces the minimum correlation coefficient (in modulus) is the best estimate of the structural index (η).

In all applications in this paper, we assigned the following structural indices η: 3, 2, 1, and 0.1 (a value close to zero).

Selecting the best vertical coordinate estimates in Euler deconvolution

According to Silva and Barbosa (2003), at the plateaus in the plots of $\hat{z}_o$, the estimates $\hat{z}_o$ are very close to the z-coordinate of the true source only if the assumed structural index is correct. After identifying the plateaus in the plots of estimates $\hat{x}_o$ and $\hat{y}_o$ (Figure 2a and 2b) and determining the best estimate of the structural index (η), we proceed to selecting the best estimates of z_o from the set of estimates obtained through Euler deconvolution using the best estimate of the structural index (η). For this, our practical procedure begins by producing a plot of all these estimates $\hat{z}_o$ against the

x- and y-coordinates of the center of the moving data window used in Euler deconvolution (not shown). Next, we determine the intersection of the sets of estimates $\hat{x}_o$ and of $\hat{y}_o$ defining plateaus (Figure 2c and 2d) and extract the subset of the estimates $\hat{z}_o$ that fall within this intersection. Finally, we compute the sample mean $\tilde{z}_o$ of the extracted subset of the estimates $\hat{z}_o$. This sample mean $\tilde{z}_o$ is taken as the best depth estimate of the source.

Geologic setting with multiple sources

The method described so far works well when applied to an isolated anomaly produced by a single source. However, in real world scenarios where the observed total-field anomaly is produced by M sources (Figure 3a), the above-described method is not sufficient to identify all plateaus. In this case, we need to identify and individualize each of the M plateaus occurring in the plots of $\hat{x}_o$ and $\hat{y}_o$ (Figure 3b) to select the best horizontal coordinate estimates of each source. To automatically map each plateau we first fit, in the least-squares sense, first-degree polynomials to estimates $\hat{x}_o$ and $\hat{y}_o$ using a moving-window scheme, and the places where the corresponding angular-coefficients estimates are closest to zero identify the plateaus of $\hat{x}_o$ and $\hat{y}_o$ (black ribbons in Figure 3b) exactly as done in the case of a single source. Then, we discriminate among the subsets of x- and y-coordinates related to each plateau using a cluster analysis algorithm (see Appendix B). After discriminating each plateau in the plots of $\hat{x}_o$ and $\hat{y}_o$, the above-explained approaches to determine the structural index and to select the best vertical coordinate estimates in Euler deconvolution are applied to each plateau as in the case of a single source.

SYNTHETIC DATA APPLICATION

We applied our method to a synthetic noise-corrupted total-field anomaly (not shown) produced by a spherical source with a radius of 1 km and by a semi-infinite horizontal cylinder with a radius of 0.2 km. The anomaly was corrupted with pseudorandom zero-mean Gaussian noise with a standard deviation of 2 nT. The two simulated sources are emplaced in a nonmagnetic medium having induced magnetization with magnetization inclination of 90° and declination of 0°. The spherical source center is located at $x_o = 20$ km, $y_o = 24$ km, and $z_o = 2$ km with magnetization intensity of 1 A/m. The horizontal cylinder has a uniform magnetization of 8 A/m, and its center is located at $x_o = 20$ km and $z_o = 2$ km whereas y_o ranges from 64 km to infinite in the y-direction. Below, we illustrate the steps of our methodology.

The first step is to estimate the horizontal source positions. To do this, we apply the Euler deconvolution using a 15×15 moving data window and assuming an arbitrary structural index. Figure 4a and 4b shows the estimates $\hat{x}_o$ and $\hat{y}_o$ against the x- and y-coordinates of the center of the moving data window. The most striking features in these maps are the overall trend of an inclined plane, and the presence of two local plateaus. Both plateaus on the map of $\hat{x}_o$ (Figure 4a) occur at $\hat{x}_o = 20$ km, which recover the true positions along x-direction. On the map of $\hat{y}_o$ (Figure 4b), the two plateaus occur at $\hat{y}_o = 24$ km and $\hat{y}_o = 64$ km, which coincide with the y-coordinates of the true simulated sources (the center of the sphere and the extremity of the semi-infinite horizontal cylinder, respectively). Notice that the extremity of the semi-infinite horizontal cylinder behaves like a 3D source.

The second step consists in identifying automatically the plateaus in the map of estimates $\hat{x}_o$ and $\hat{y}_o$. After estimating $\hat{x}_o$ and $\hat{y}_o$, we fit in the least-squares sense a first-degree polynomial to these estimates by using a moving window of 15×15 grid points (see Appendix A). Figure 4c and 4d shows the estimated x- and y-coefficients of the polynomial ($\hat{c}_x$ and $\hat{c}_y$) against the x- and y-coordinates of the moving-window center. In both maps of $\hat{c}_x$ (Figure 4c) and $\hat{c}_y$ (Figure 4d) against the x- and y-coordinates of the moving-window center, we highlighted the areas associated with estimated angular coefficients closest to zero values (white areas in Figure 4c and 4d), which locate the plateaus of $\hat{x}_o$ (Figure 4a) and $\hat{y}_o$ (Figure 4b), respectively. To automatically identify the subsets of the x- and y-coordinates related to each plateau on the maps of $\hat{x}_o$ and $\hat{y}_o$, we employed a clustering algorithm (see Appendix B). This procedure discriminates between two subsets of the x- and y-coordinates (not shown) which define the positions of the two plateaus in the maps of $\hat{x}_o$ and $\hat{y}_o$.

In the third step of our method, we obtain the best estimates of the horizontal positions of each source. After identifying the plateaus in
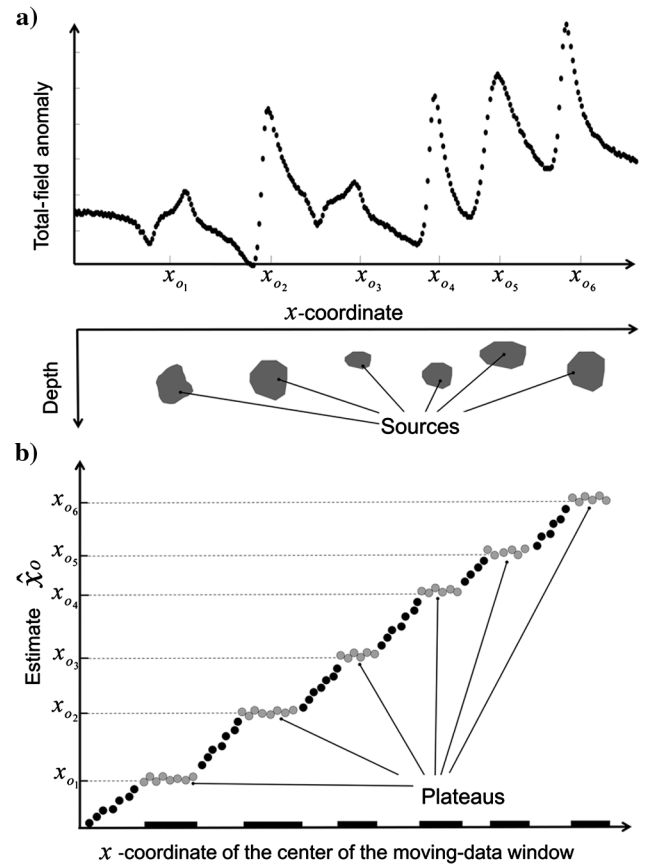

Figure 3. Two-dimensional schematic representation of (a) the total-field anomaly (dots) produced by six sources (gray polygons in the lower panel) whose locations are x_{o_j}, $j = 1, \ldots, 6$. (b) Estimates $\hat{x}_o$ (dots) against the x-coordinate of the center of the moving-data window. The estimates of $\hat{x}_o$ define inclined planes (black dots) and six plateaus (gray dots), each one associated with estimates $\hat{x}_o$ nearly constant and close to the x-coordinates of a true source (x_{o_j}, $j = 1, \ldots, 6$). The black ribbons pinpoint the subsets of x-coordinates which locate the plateaus.

the plots of $\hat{c}_x$ and $\hat{c}_y$, we extract the subsets of the $\hat{x}_o$ and $\hat{y}_o$ estimates that fall within the respective plateaus. Then, we compute the sample means $\tilde{x}_o$ and $\tilde{y}_o$ of the respective subsets of the $\hat{x}_o$ and $\hat{y}_o$ estimates that will be taken as the best estimate of the source position along the x- and y-directions. Because there are two plateaus on the maps of $\hat{x}_o$ and $\hat{y}_o$, there will be two sample means of

the estimates $\hat{x}_o$ and $\hat{y}_o$ calculated over each plateau which are the best estimates of the horizontal source positions ($\tilde{x}_o$ and $\tilde{y}_o$). By comparing the two sample means $\tilde{x}_o$ and $\tilde{y}_o$ with the respective true values (Table 1), we certify the good performance of our method in recovering the best estimates of the horizontal source positions in Euler deconvolution.
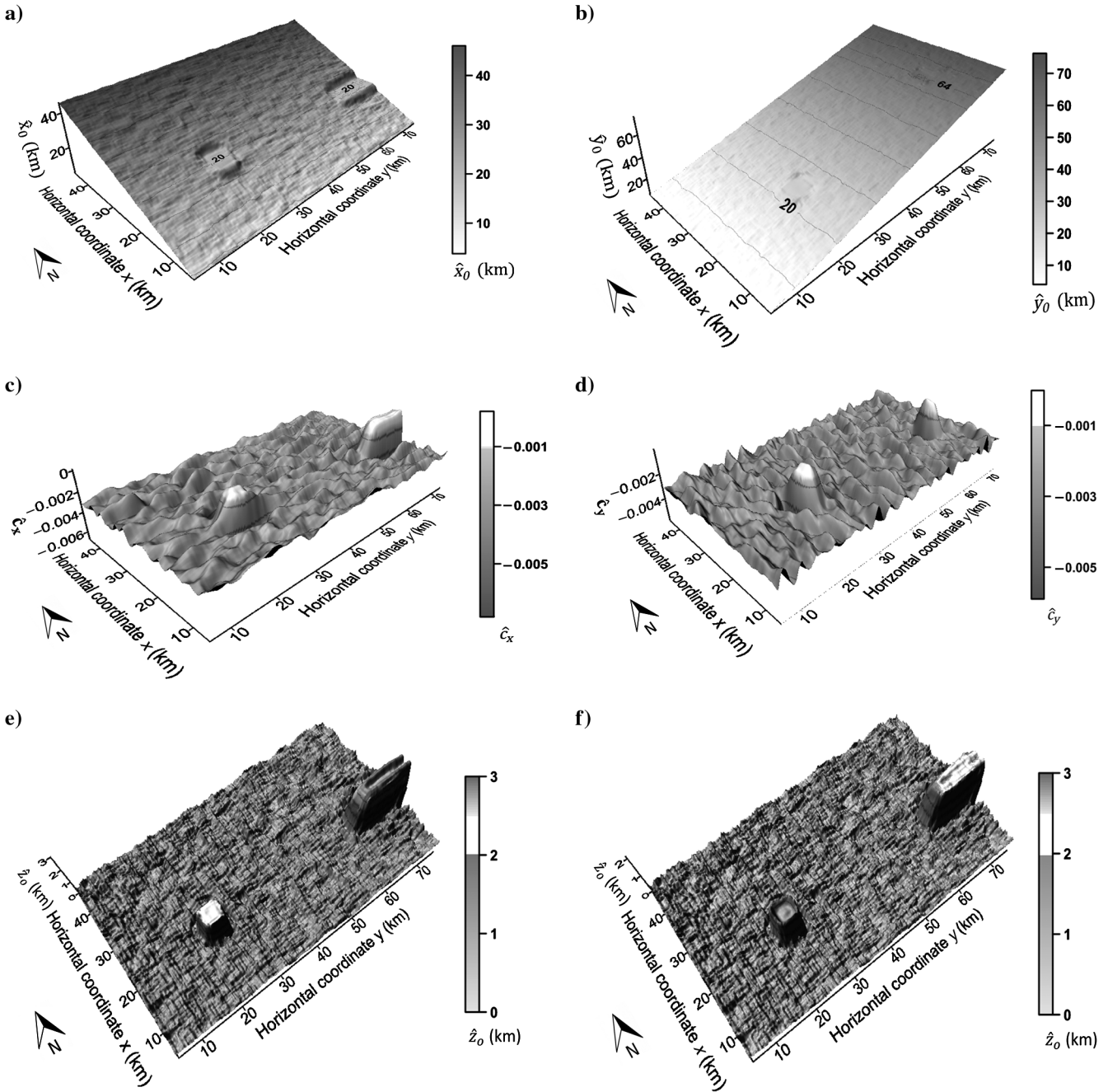

Figure 4. Synthetic data test produced by sources with different geometries. The westernmost and easternmost sources are, respectively, a sphere and a semi-infinite horizontal cylinder, both with 2-km-deep centers. Estimates (a) $\hat{x}_o$ and (b) $\hat{y}_o$ against the x- and y-coordinates of the center of the moving data window in Euler deconvolution. Estimates of angular coefficients (c) $\hat{c}_x^k$ and (d) $\hat{c}_y^k$ against the x- and y-coordinates of the center of a kth moving window which spans the maps of the estimates of $\hat{x}_o$ and $\hat{y}_o$, respectively. The white areas in (c and d) highlight the places where, respectively, $\hat{c}_x^k$ and $\hat{c}_y^k$ are closest to zero. Estimates $\hat{z}_o$ against the x- and y-coordinates of the center of the moving data window in Euler deconvolution by assuming (e) $\eta = 3$ and (f) $\eta = 2$. The white areas in (e and f) highlight the estimates $\hat{z}_o$ that will be selected to compute the best depth estimates of the sphere and semi-infinite horizontal cylinder, respectively.

The fourth step consists in determining the structural index of each source. Thus, we select the subsets (areas) of the total-field anomaly and estimates $\hat{b}$ that approximately fall within the plateaus identified in the maps of $\hat{x}_o$ and $\hat{y}_o$. Finally, for each source, we take as the best estimate of the structural index (η) the one that produces the minimum correlation coefficient between the corresponding subset of the total-field anomaly and the estimated base level. The tentative values for the structural indices that produce the smallest correlations, in absolute values, are: (1) $\eta = 3$ in the case of the westernmost source, consistent with a dipole source (Figure 4) and (2) $\eta = 2$ in the case of the easternmost source (Figure 4). The simulated easternmost source is a semi-infinite horizontal cylinder; thus, it is not a line of dipoles, that is, the structural index is not $\eta = 2$. For most of the area, however, just from inspection of the Euler solutions (Figure 4), we can easily infer that this easternmost source behaves like a 2D source (infinite horizontal cylinder with $\eta = 2$). Thus, the estimated index $\eta = 2$ (line of dipoles) will be accepted as the correct one because it yields a minimum correlation.

In the fifth step, we obtain the best estimates of the vertical positions of each source. To this end, we apply the Euler deconvolution assuming the estimated indices as the true ones to estimate the coordinate $\hat{z}_o$ for each source. The maps of the estimates $\hat{z}_o$ against the x- and y-coordinates of the center of the moving data window by assuming $\eta = 3$ and $\eta = 2$ are shown in Figure 4e and 4f, respectively. To estimate the best $\hat{z}_o$ for each source, we pick out those estimates $\hat{z}_o$ (Figure 4e and 4f) over the intersections of the pairs of mapped plateaus of $\hat{x}_o$ and of $\hat{y}_o$. The white areas (Figure 4e and 4f) highlight the estimates $\hat{z}_o$ lying at the intersections (not shown) of the pairs of mapped plateaus of $\hat{x}_o$ and of $\hat{y}_o$. The two subsets of estimates $\hat{z}_o$ (in white, Figure 4e and 4f) were used to compute the two sample means $\tilde{z}_o$, each one associated with one of the simulated magnetic sources (sphere and semi-infinite horizontal cylinder, respectively). These sample means of $\hat{z}_o$ are: (1) $\tilde{z}_o = 2.07$ km in the case of the sphere (the westernmost source in Figure 4e) and (2) $\tilde{z}_o = 2.05$ km in the case of the semi-infinite horizontal cylinder (the easternmost source in Figure 4f). These sample means $\tilde{z}_o$ are taken as the best depth estimates of these sources, being consistent with the true depths of the simulated sources (Table 1).

INTERFERING SIGNALS

In this section, we investigate the sensitivity of our method when used to interpret interfering anomalies produced by sources that are horizontally separated from each other by short distances. We analyze the ability of our method to correctly recover the horizontal and vertical source positions in the case of weak-, mid-, and strong-interfering signals. To conduct this analysis, we use the same simulated sources described in the previous section. We kept the original variables describing the sphere and the semi-infinite horizontal cylinder, except for their horizontal coordinate y_o (east–west source positions), which will be modified to reduce the distance between the sources. The sensitivity is studied as a function of separation-to-depth ratio (d/z_o), where d is the horizontal distance between the sources, measured along the y-direction (east-west direction). To do this, d is gradually reduced, giving rise to total-field anomalies ranging from weakly to strongly interfering.

We computed six noise-corrupted total-field anomalies (Figure 5). The anomalies were corrupted with pseudorandom zero-mean Gaussian noise with a standard deviation of 2 nT. In the first test, the d/z_o ratio is equal to 10 with the sphere and semi-infinite

horizontal cylinder located at $y_o = 34$ km and $y_o = 54$ km, respectively. This test simulates weakly interfering anomalies (Figure 5a). In the next tests, the sources are gradually placed closer to each other. To do this, the d/z_o ratio is decreased by subtracting two units from its current value until $d/z_o = 1$. In the last test, strongly interfering anomalies (Figure 5f) are produced by the sphere and the semi-infinite horizontal cylinder which are located at $y_o = 43$ km and $y_o = 45$ km, respectively.

We apply the Euler deconvolution to each magnetic data set shown in Figure 5. At this stage, aiming at estimating just the horizontal source positions, we use a 15×15 moving data window and assume any structural index. By applying our method that automatically identifies the plateaus on the maps of $\hat{x}_o$ and $\hat{y}_o$ and determines the best estimates of the horizontal source positions, we note that the estimates $\tilde{x}_o$ and $\tilde{y}_o$ are good in the case of weak- and midinterfering anomalies (d/z_o varying from 10 to 2, in Figure 5a–5e); however, it fails in the case of strong-interfering anomalies ($d/z_o = 1$, in Figure 5f) as shown in Table 2.

To obtain the best depth estimates, we first need to determine the structural index for each source. To do this, for each source, we compute the correlation coefficients between the total-field anomaly and the estimate base level by assigning several tentative values to the structural index following the same procedure adopted in the previous section. By assuming different structural indices, we compute the correlation coefficients computed over the anomalies located at the westernmost (Figure 6a) and easternmost (Figure 6b) portions of the area. In the case of weak- and midinterfering anomalies (d/z_o varying from 10 to 2) the smallest correlation coefficients over the westernmost and easternmost anomalies occur for $\eta = 3$ (Figure 6a) and $\eta = 2$ (Figure 6b), respectively. These results show excellent agreement with the true simulated sources: the westernmost source is a sphere (or a dipole with $\eta = 3$) and the easternmost one is a semi-infinite horizontal cylinder (or a source that behaves like a line of dipoles with $\eta = 2$ for most of the area). However, the structural indices are wrongly determined in the case of strong interfering anomalies where $d/z_o = 1$. In this case where $d/z_o = 1$, the smallest correlation coefficients over the westernmost and easternmost anomalies occur for $\eta = 2$ (Figure 6a and 6b).

After determining these two structural indices, we apply the Euler deconvolution assuming the determined structural indices to obtain the best depth estimates. Table 2 shows the six depth estimates $\tilde{z}_o$, each one obtained for a fixed d/z_o ratio. A noticeable aspect of these depth estimates is that they show close agreement with the true ones ($z_o = 2$ km) in the case of weak- and mid-interfering anomalies (Figure 5a–5e). However, in the case of strong-interfering anomalies (Figure 5f) where $d/z_o = 1$, the structural indices are

Table 1. Horizontal and vertical coordinates of true spherical and cylindrical sources (x_o, y_o, z_o) and the best estimates of the horizontal and vertical coordinates ($\tilde{x}_o, \tilde{y}_o, \tilde{z}_o$). The coordinate y_o of the cylinder refers to its extremity.

Source	x_o (km)	y_o (km)	z_o (km)	$\tilde{x}_o$ (km)	$\tilde{y}_o$ (km)	$\tilde{z}_o$ (km)
Sphere ($\eta = 3$)	20	24	2.0	20.00	24.01	2.05
Cylinder ($\eta = 2$)	20	64	2.0	19.99	64.01	1.99

wrongly determined and thus the best depth estimates over the westernmost and easternmost sources are wrongly estimated.

Additional synthetic examples are illustrated in the supplementary material of Melo et al. (2013).

REAL DATA APPLICATION

Figure 7 shows the aeromagnetic total-field anomaly over mafic-ultramafic alkaline bodies, in central Brazil (Dutra and Marangoni,

2009). The flight height was 150 m above the ground surface. The strong magnetic anomalies at the southwestern and northeastern quadrants of the study area have been identified by Brasil (1974), and named *Morro do Engenho* and A2 anomalies, respectively. The Morro do Engenho Complex anomaly is produced by an alkaline outcropping body intruded in sediments. This plutonic body presents concentric layered structures in which the inner layer is composed of dunites, the intermediate layer consists of peridotites and pyroxenites and the outer layer is made up of alkaline gabbro
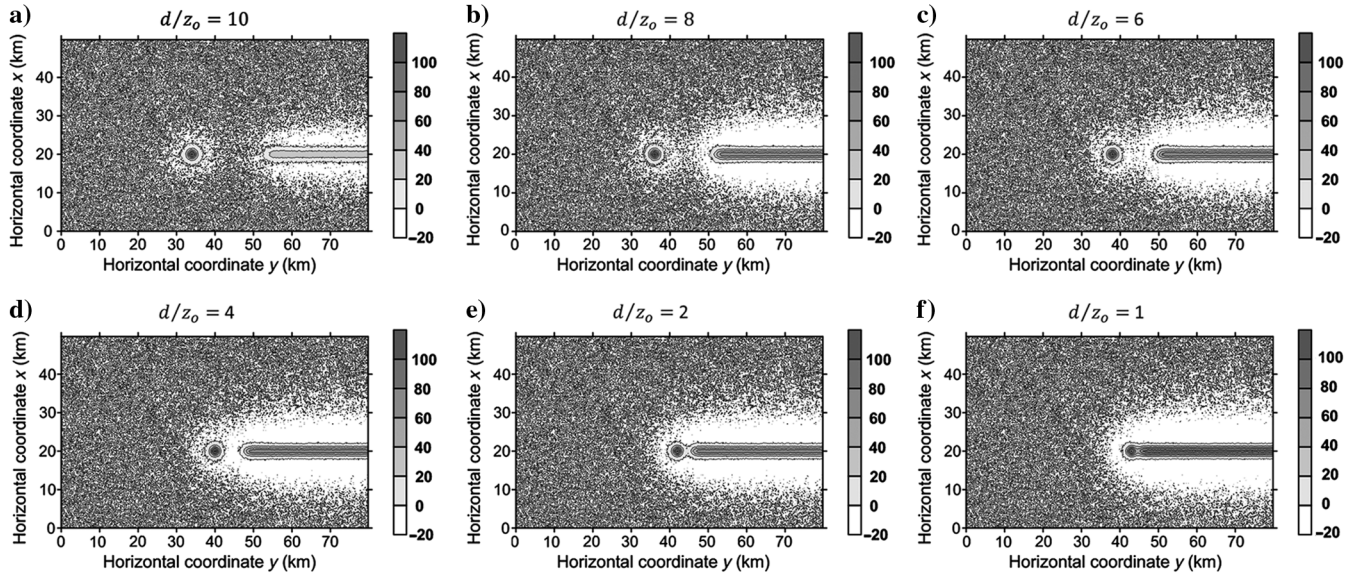

Figure 5. Analysis of the sensitivity to interpret interfering anomalies as a function of separation-to-depth ratio (d/z_o). Noise-corrupted total-field anomalies produced by a sphere and a semi-infinite horizontal cylinder located, respectively, at the center and at the easternmost limit of the data. The centers of these sources are at the same depth of $z_o = 2$ km and at the same horizontal coordinate $x_o = 20$ km. The variation of the separation distance d between the sources along the y-direction (east–west direction) is expressed in terms of variations in d/z_o spanning the values (a) 10, (b) 8, (c) 6, (d) 4, (e) 2, and (f) 1.

Table 2. Analysis of the sensitivity in interpreting interfering anomalies as a function of separation-to-depth ratio (d/z_o), where d is the horizontal separation distance between the sources that is measured along the y-direction (east–west direction). Horizontal and vertical coordinates of true spherical and cylindrical sources (x_o, y_o, z_o) and the best estimates of the horizontal and vertical coordinates ($\tilde{x}_o, \tilde{y}_o, \tilde{z}_o$).

Source	d/z_o	x_o (km)	y_o (km)	z_o (km)	$\tilde{x}_o$ (km)	$\tilde{y}_o$ (km)	$\tilde{z}_o$ (km)
Sphere	10	20	34	2.0	20.02	33.99	2.07
Sphere	8	20	36	2.0	19.99	36.00	2.05
Sphere	6	20	38	2.0	20.00	37.99	2.02
Sphere	4	20	40	2.0	20.00	39.96	2.04
Sphere	2	20	42	2.0	19.98	41.89	2.06
Sphere	1	20	43	2.0	20.01	42.79	2.15
Cylinder	10	20	54	2.0	19.99	53.98	2.01
Cylinder	8	20	52	2.0	19.99	51.92	2.02
Cylinder	6	20	50	2.0	19.99	49.89	1.99
Cylinder	4	20	48	2.0	19.99	47.94	2.03
Cylinder	2	20	46	2.0	20.00	46.05	2.01
Cylinder	1	20	45	2.0	19.99	43.55	1.40

and syenite (Radaelli, 2000). The northeastern anomaly (A2) is a possible buried alkaline body being overlaid by the Quaternary sediments (Brasil, 1974).

To obtain the best estimates of the horizontal source positions of these alkaline bodies, we apply the Euler deconvolution using a 15×15 moving data window spanning the area limited by $x \in$ [3 km, 38 km] and $y \in$ [3 km, 42 km]. By assuming any structural index, we estimate $\hat{x}_o$ (Figure 8a) and $\hat{y}_o$ (Figure 8b) against the x- and y-coordinates of the center of the moving data window. Two plateaus are easily detected by visual inspection of the estimated maps of $\hat{x}_o$ and $\hat{y}_o$ (Figure 8a and 8b).

After estimating the maps of $\hat{x}_o$ and $\hat{y}_o$ and performing a visual analysis of the plateaus in these maps, we fit first-degree polynomials to $\hat{x}_o$ and $\hat{y}_o$ by using a moving data window of 3×3 grid points which spans the area limited by $x \in$ [11.4 km, 29.5 km] and $y \in$ [11.1 km, 33.5 km]. Figure 8c and 8d shows the estimated angular coefficients $\hat{c}_x$ and $\hat{c}_y$, against the x- and y-coordinates of the moving-window center. We can easily identify areas (in white) where $\hat{c}_x$ (Figure 8c) and $\hat{c}_y$ (Figure 8d) are closest to zero. These white areas in Figure 8c and 8d define the two subsets of the x- and y-coordinates which will be used to define the positions of the two plateaus on the maps of $\hat{x}_o$ and $\hat{y}_o$. After locating these plateaus, we compute the two sample means $\tilde{x}_o$ and $\tilde{y}_o$ of the two subsets of the $\hat{x}_o$ and $\hat{y}_o$ estimates lying over each plateau. These sample means are the best estimates of the horizontal source positions of the Morro do Engenho and A2 bodies (Table 3). After estimating the best horizontal source positions, we estimate the structural index of each body following the same procedure adopted in the previous test. Both bodies are interpreted as dipoles (spheres) because the tentative values for the structural indices that produce the smallest correlation coefficients between the total-field anomaly and the estimated base level computed around the Morro do Engenho and A2 bodies are equal to 3. Because the best estimate of the structural index is the same for both sources, we produce only one map of the estimates $\hat{z}_o$ against the x- and y-coordinates of the center of the moving data window (Figure 8e). To estimate the best $\tilde{z}_o$ we compute, for each source, the sample averages of the respective estimates $\hat{z}_o$ located over the intersections (not shown) of the pairs of plateaus of $\hat{x}_o$ and of $\hat{y}_o$. As shown in Table 3, Morro do Engenho and A2 bodies are two sphere-like sources whose centers are located at depths of 3 and 3.2 km, respectively.

Morro do Engenho and A2 bodies are located on the northern part of Goiás Alkaline Province, which results from mafic-alkaline magmatism occurred in Late Cretaceous along a northwest–southeast lineament (Dutra et al., 2012). This alkaline province has been studied by several authors, who proposed two hypotheses about the shape of the igneous intrusions and the mechanisms responsible for their emplacement. The first hypothesis advocates that the alkaline bodies are plug-like intrusions that cut the crust by taking advantage of prior weakness zones (e.g., fractures and faults) where

the mobile material is driven into (Gomes et al., 1990; Danni, 1994). The second hypothesis advocates that the alkaline bodies are sphere-like intrusions being consistent with the model of magmatic chambers instead of plug intrusions (Junqueira-Brod et al., 2005; Dutra and Marangoni, 2009). Junqueira-Brod et al. (2005) propose that plutonic bodies were intruded along the contact between the Precambrian basement and the sedimentary rocks. This unconformity has allowed enough space to accommodate relatively large amounts of magma, yielding magmatic chambers. On the other hand, Dutra et al. (2012) suggest that the Morro do Engenho complex have spherical shape whereas the A2 anomaly would have the shape of a vertical cylinder (plug). Our result agrees with the hypothesis of sphere-like intrusions because the estimated structural indices for Morro do Engenho and A2 bodies are the same and
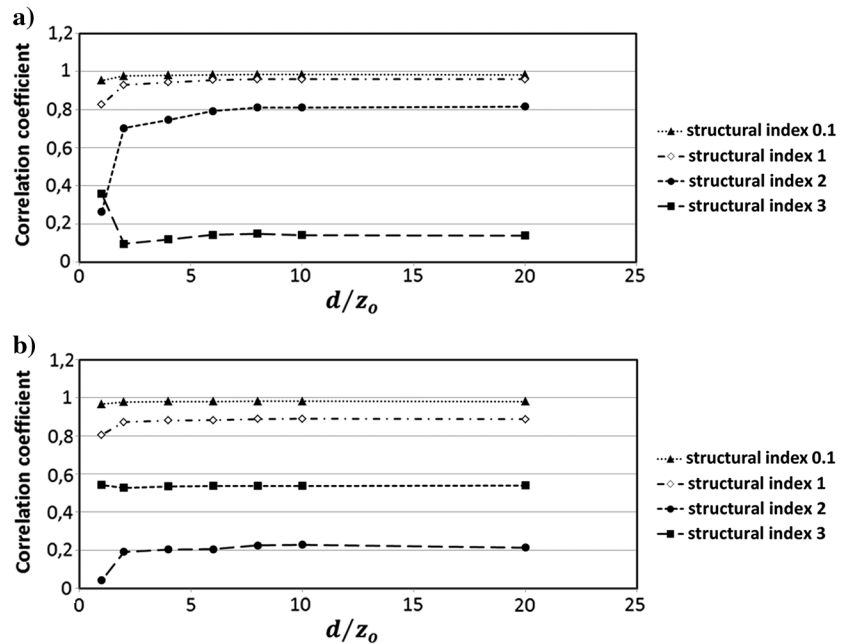
Figure 6. Correlation coefficients between the total-field anomaly and the estimated base level for different values of the tentative structural index versus d/z_o. These coefficients are computed over the anomalies located at the (a) westernmost and (b) easternmost portions of the area.
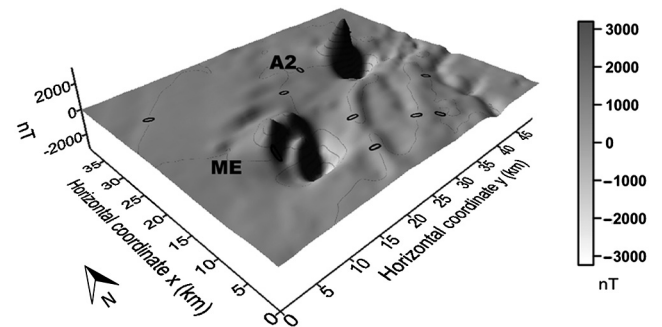
Figure 7. Alkaline bodies, Brazil: Total-field anomaly. Morro do Engenho and A2 anomalies are pinpointed as ME and A2, respectively.

Table 3. Real data application. Best estimates of the horizontal and vertical coordinates $(\tilde{x}_o, \tilde{y}_o, \tilde{z}_o)$ of two alkaline sources.

Source	$\tilde{x}_o$ (km)	$\tilde{y}_o$ (km)	$\tilde{z}_o$ (km)
Morro do Engenho (ME)	11.50	15.40	3.20
Anomaly A2	23.83	36.35	2.97

equal to the index of a dipole (sphere). However, the hypothesis of plug-like intrusions cannot be discarded. If the bodies have the thickness comparable to the width, like an equilateral cylinder, the Euler deconvolution cannot distinguish the equilateral cylinder from a sphere.

CONCLUSIONS

We have presented a new method for selecting the best source location estimates in Euler deconvolution. Our approach has drastically reduced the number of the selected Euler solutions to a single
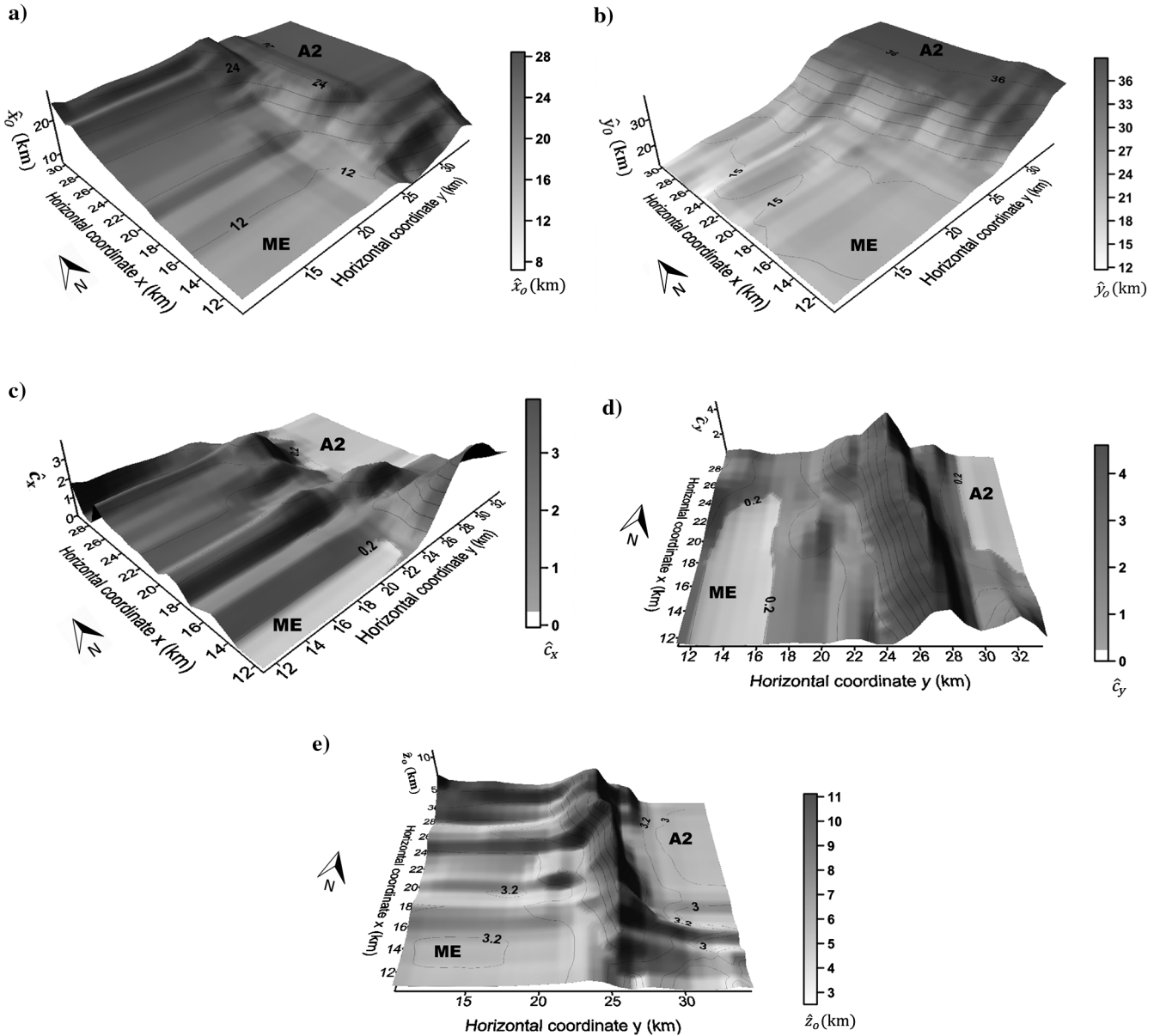
Figure 8. Alkaline bodies, Brazil: Estimates (a) $\hat{x}_o$ and (b) $\hat{y}_o$ against the x- and y-coordinates of the center of the moving data window in Euler deconvolution. Estimates of the angular coefficients (c) $\hat{c}_x^k$ and (d) $\hat{c}_y^k$ against the x- and y-coordinates of the center of a kth moving window which spans the maps of the estimates of $\hat{x}_o$ and $\hat{y}_o$, respectively. The white areas in (c and d) highlight the places where, respectively, $\hat{c}_x^k$ and $\hat{c}_y^k$ are closest to zero. (e) Estimates $\hat{z}_o$ against the x- and y-coordinates of the center of the moving data window in Euler deconvolution by assuming $\eta = 3$. The white areas in (e) highlight the estimates $\hat{z}_o$ that will be selected to compute the best depth estimates of the alkaline bodies. ME and A2 pinpoint the alkaline positions of Morro do Engenho and A2, respectively.

one per anomaly. This is possible because our method does not select Euler solutions based on their statistical consistency after a cluster analysis. Rather, in our method, this selection is grounded on the theoretical analysis of the estimators for the horizontal and vertical source positions in Euler deconvolution as a function of the x- and y-coordinates of the observations. Our approach consists in detecting automatically the regions of the anomaly producing consistent estimates of the source horizontal coordinates. These regions form plateaus in the horizontal coordinates estimates. We automatically identify these plateaus by fitting a first-degree polynomial to the horizontal coordinate estimates with a moving-window operator which spans these estimates. The places where the angular-coefficients estimates are closest to zero identify automatically the plateaus of the horizontal coordinate estimates where consistent estimates of the horizontal source positions are found. In our method, the best estimates of the horizontal source positions are the sample means of the estimates that fall within the respective plateaus. After estimating the structural index for each source, we apply the Euler deconvolution using the estimated structural index and assume as the best estimates of the vertical source positions the sample means of the estimates that fall at the intersections of the pairs of plateaus associated with each horizontal coordinate estimates. Tests using synthetic and real data showed that our method is able to correctly estimate the source locations whether the sources geometries (structural indices) are the same.

The cornerstone of our method's ability to automatically select the best estimates of the horizontal source positions is its capacity to recognize the plateaus in the horizontal coordinate estimates. We identify the plateaus by fitting a first-degree polynomial to the horizontal coordinate estimates. However, other methodologies could be employed such as the pattern recognition techniques (e.g., neural networks, template matching, discriminant analysis, principal component analysis, and support vector machine). To determine the best depth estimate for each source, we need to estimate the structural index, we stress that other methods besides the proposed one could also be employed.

The main limitation of our method is its limited performance in interpreting 2D sources. This occurs because, along the strike of a 2D source, the horizontal coordinate estimates vary and then the plateaus are not well defined. Moreover, our approach inherits the same limitations of Euler deconvolution. The first one is its poor performance in interpreting interfering anomalies produced by multiple sources that are vertically (or horizontally) separated from each other by short distances. The second limitation is its modest performance in interpreting noisy data.

In contrast with other strategies for accepting Euler solutions, our method does not use statistical and clustering procedures. Hence, our method is less sensitive to the presence of noise in the data. Moreover, our method does not require that the anomaly be reduced to the pole to enhance the highest absolute values of the anomalies.

ACKNOWLEDGMENTS

APPENDIX A

THE MATHEMATICAL DETAILS FOR SELECTING THE BEST HORIZONTAL COORDINATE ESTIMATES OF THE SOURCE IN EULER DECONVOLUTION

The practical procedure to differentiate the plateaus from inclined planes on the estimates $\hat{x}_o$ and $\hat{y}_o$ is as follows. First, we set a regular grid of $NX \times NY$ points of a moving window that will sweep the map of estimates $\hat{x}_o$ with a shift of one grid unit. Here, NX and NY are the numbers of estimates $\hat{x}_o$ along the x- and y-directions, respectively. The total number of points (estimates $\hat{x}_o$) defining a moving window is $N = NX \cdot NY$. Then, a subset of the estimates $\hat{x}_o$, within the kth moving window, is fitted in the least-squares sense by a first-degree polynomial in both x- and y-directions, i.e.,

$$x_{o_i}^k = c_o^k + c_x^k x_i^k + c_y^k y_i^k, \qquad i = 1, \dots, N. \qquad \text{(A-1)}$$

This linear relationship can be written in matrix notation as

$$\mathbf{x_o}^k = \mathbf{A}^k \mathbf{c}^k, \qquad \text{(A-2)}$$

where $\mathbf{x_o}^k$ is an N-dimensional vector containing the subset of estimates $\hat{x}_o$ within the kth moving window, $\mathbf{c}^k \equiv (c_o^k, c_x^k, c_y^k)^T$ is a vector containing the three unknown coefficients of the first-degree polynomial of the kth moving window, and $\mathbf{A}^k$ is an $N \times 3$ matrix whose columns are N-dimensional vectors given by: $\mathbf{a}_1^k \equiv (1, \dots, 1)^T$, $\mathbf{a}_2^k \equiv (x_1^k, \dots, x_i^k, \dots, x_N^k)^T$, and $\mathbf{a}_3^k \equiv (y_1^k, \dots, y_i^k, \dots, y_N^k)^T$, where x_i^k and y_i^k are the x- and y-coordinates defining the position of the ith estimate $\hat{x}_{o_i}^k$.

Next, we obtain estimates $\hat{c}_o^k, \hat{c}_x^k$ and $\hat{c}_y^k$ as least-squares solution of equation A-2. We repeat this procedure for each position of a moving window spanning the estimates $\hat{x}_o$, with a shift of one grid unit. In practice, we use the same window size that was used in applying the Euler deconvolution. If the number of Euler solutions is reduced, we can use a smaller window size than the one used in Euler deconvolution. The best estimates of $\hat{x}_o$ are those related to the estimated coefficients $\hat{c}_x^k$ that are closest to zero. These coefficients are used to map the plateaus of $\hat{x}_o$, where consistent estimates of the horizontal source positions in Euler deconvolution are very close to the true ones. Notice that each estimated coefficient $\hat{c}_x^k$ is located at the x- and y-coordinates of the kth moving-window center. These estimates are then used to compute the sample mean $\tilde{x}_o$ of the estimates $\hat{x}_o$, which is assumed to be the best estimate of the source position along the x-direction. Mutatis mutandis, this practical procedure is repeated for the estimates $\hat{y}_o$.

APPENDIX B

DETAILS FOR DEFINING THE SUBSETS OF HORIZONTAL COORDINATES OF EACH PLATEAU

By assuming a set of M laterally adjacent sources, we can automatically map M plateaus in the plots of the estimates $\hat{c}_x$ and $\hat{c}_y$ closest to zero (Appendix A). The position of each plateau in these plots is defined by a subset of x- and y-coordinates that defines a cluster. Our clustering algorithm identifies those x- and y-coordinates that are closest to each other following a distance criterion. The algorithm is based in the premise that a circle in the $x - y$ space with the radius r chosen by the user and centered at any pair (x_i, y_i) defines a cluster. For each point (x_i, y_i), we create a circle with radius r centered at the point. Then, all the points within the same circle are classified as belonging to the same cluster. Let us assume that two points are spatially separated from each other by a distance of 0.5 m, if the user defines $r = 1$ m; then, these points will be classified as belonging to the same cluster because a circle of $r = 1$ m is centered at each point.

REFERENCES

Brasil, 1974. Departamento Nacional de Produção Mineral. Mapa de interpretação magnética, Projeto Iporá; escala 1:250.000. Prospec S.A.

Barbosa, V. C. F., and J. B. C. Silva, 2011, Reconstruction of geologic bodies in depth associated with a sedimentary basin using gravity and magnetic data: Geophysical Prospecting, **59**, 1021–1034, doi: 10.1111/j.1365-2478.2011.00997.x.

Barbosa, V. C. F., J. B. C. Silva, and W. E. Medeiros, 1999, Stability analysis and improvement of structural index estimation in Euler deconvolution: Geophysics, **64**, 48–60, doi: 10.1190/1.1444529.

Danni, J. C. M., 1994, Os picritos alcalinos da região de Iporá: Implicaçães na gênese dos complexos do tipo central do sul de Goiás: Revista Brasileira de Geociências, **24**, 112–119.

Dutra, A. C., and Y. R. Marangoni, 2009, Gravity and magnetic 3-D inversion of Morro do Engenho complex, central Brazil: Journal of South American Earth Sciences, **28**, 193–203, doi: 10.1016/j.jsames.2009.02.006.

Dutra, A. C., Y. R. Marangoni, and T. C. Junqueira-Brod, 2012, Investigation of the Goiás Alkaline Province, Central Brazil: Application of gravity and magnetic methods: Journal of South American Earth Sciences, **33**, 43–55, doi: 10.1016/j.jsames.2011.06.004.

Fairhead, J. D., K. J. Bennett, D. R. H. Gordon, and D. Huang, 1994, Euler: Beyond the "black box": 64th Annual International Meeting, SEG, Expanded Abstracts, 422–424.

FitzGerald, D., A. B. Reid, and P. McInerney, 2004, New discrimination techniques for Euler deconvolution: Computers & Geosciences, **30**, 461–469, doi: 10.1016/j.cageo.2004.03.006.

Gomes, C. B., E. Ruberti, and L. Morbidelli, 1990, Carbonatite complexes from Brazil: A review: Journal of South American Earth Sciences, **3**, 51–63, doi: 10.1016/0895-9811(90)90017-U.

Jekeli, C., 2009, On methods to select solutions in Euler deconvolution of gravitation and gradient measurements: Studia Geophysica et Geodaetica, **53**, 443–457, doi: 10.1007/s11200-009-0033-7.

Junqueira-Brod, T. C., J. C. Gaspar, J. A. Brod, H. Jost, E. S. R. Barbosa, and C. V. Kafino, 2005, Emplacement of kamafugite lavas from the Goiás alakaline province, Brazil: Constrains from whole-rock simulations: Journal of South American Earth Sciences, **18**, 323–335, doi: 10.1016/j.jsames.2004.11.001.

Li, X., 2003, On the use of different methods for estimating magnetic depth: The Leading Edge, **22**, 1090–1099, doi: 10.1190/1.1634912.

Melo, F. F., V. C. F. Barbosa, L. Uieda, V.C. Oliveira, Jr., and J. B. C. Silva, 2013, Supplementary material to "Estimating the nature and the horizontal and vertical positions of 3D magnetic sources using Euler deconvolution". 10.6084/m9.figshare.649433, accessed 22 March 2013.

Mikhailov, V., A. Galdeano, M. Diament, A. Gvishiani, S. Agayan, S. Bogoutdinov, E. Graeva, and P. Sailhac, 2003, Application of artificial intelligence for Euler solutions clustering: Geophysics, **68**, 168–180, doi: 10.1190/1.1543204.

Radaelli, V. A., 2000, Programa levantamentos geológicos básicos do Brasil. Geologia e recursos minerais do Estado de Goiás e do Distrito Federal. Informe de recursos minerais, Níquel do Morro do Engenho — Estado de Goiás. — Goiânia, CPRM, 10.

Ravat, D., 1996, Analysis of the Euler method and its applicability in environmental magnetic investigations: Journal of Environmental and Engineering Geophysics, **1**, 229–238, doi: 10.4133/JEEG1.3.229.

Reid, A. B., J. M. Allsop, H. Granser, A. J. Millet, and I. W. Somerton, 1990, Magnetic interpretation in three dimensions using Euler deconvolution: Geophysics, **55**, 80–91, doi: 10.1190/1.1442774.

Silva, J. B. C., and V. C. F. Barbosa, 2003, 3D Euler deconvolution: Theoretical basis for automatically selecting good solutions: Geophysics, **68**, 1962–1968, doi: 10.1190/1.1635050.

Silva, J. B. C., V. C. F. Barbosa, and W. E. Medeiros, 2001, Scattering, symmetry, and bias analysis of source-position estimates in Euler deconvolution and its practical implications: Geophysics, **66**, 1149–1156, doi: 10.1190/1.1487062.

Thompson, D. T., 1982, EULDPH: A new technique for making computer assisted depth estimates from magnetic data: Geophysics, **47**, 31–37, doi: 10.1190/1.1441278.

Ugalde, H., and W. A. Morris, 2010, Cluster analysis of Euler deconvolution solutions: New filtering techniques and geologic strike determination: Geophysics, **75**, no. 3, L61–L70, doi: 10.1190/1.3429997.